

Quaternary MgSiN₂-GaN alloy semiconductors for deep UV applications

Ozan Dernek* and Walter R. L. Lambrecht†

*Department of Physics, Case Western Reserve University,
10900 Euclid Avenue, Cleveland, OH-44106-7079*

Ultra-wide direct band gap semiconductors hold great promise for deep ultraviolet opto-electronic applications. Here we evaluate the potential of MgSiN₂-GaN alloys for this purpose. Although MgSiN₂ itself has an indirect gap ~ 0.4 eV below its direct gap of ~ 6.5 eV, its different sign lattice mismatch from GaN in two different basal plane directions could avoid the tensile strain which limits Al_xGa_{1-x}N on GaN for high x . Two octet-rule preserving structures (with space groups $Pmn2_1$ and $P1n1$) of a 50 % alloy of MgSiN₂ and GaN are investigated and are both found to have gaps larger than 4.75 eV using quasiparticle self-consistent (QS) *GW* calculations. Both are nearly direct gap in the sense that the indirect gap is less than 0.1 eV lower than the direct gap. Their mixing energies are positive yet small, with values of 8 (31) meV/atom for $Pmn2_1$ ($P1n1$) indicating only a small driving force toward phase separation.

I. INTRODUCTION

Compact light sources in the deep UV, in particular the UV-B and UV-C with wavelengths shorter than 315 nm and 280 nm respectively would have a large impact in science and technology [1]. Light emitting diodes (LED) in this range could fulfill this demand but require new semiconductor materials with efficient doping and band gaps $E_g > 4$ eV. The current prevailing approach toward this goal is to develop Al_xGa_{1-x}N alloys, which form a continuous alloy system with wurtzite structure and end point band gaps of 3.6 eV (GaN) and 6.3 eV (AlN). [2–6] However, high Al-content alloys suffer from a number of challenges: (1) epitaxial growth on GaN substrates results in tensile strain, which tends to develop cracks, (2) n-type doping with Si leads to distorted DX center with a deep level and hence inefficient doping, (3) p-type doping is even more problematic and (4) the inverted crystal field splitting of AlN leads to predominantly transverse magnetic (TM) light emission from the basal plane surface.[7, 8] Here we propose alloys of MgSiN₂ and GaN as an alternative to overcome at least some of these problems.

Heterovalent ternary semiconductors of the type II-IV-N₂ using group II and group-IV element pairs as a replacement for the group III element in III-N nitrides, have gained significant interest in recent years.[9–11] These materials have a wurtzite derived structure, which ideally consists in a fully ordered orthorhombic superlattice of wurtzite with space group #33 (Pbn_1 in the setting with $a_o \approx 2a_w, b_o \approx \sqrt{3}a_w, c_o = c_w$ where a_w, c_w are the wurtzite and a_o, b_o, c_o the orthorhombic lattice constants, or $Pna2_1$ if a_o and b_o are reversed). They add significant flexibility to the chemical materials design space because one has a choice of II=Be, Mg, Zn, Cd and IV= Si, Ge, Sn. Furthermore, a certain degree of

polytypic disorder with space group #26 ($Pmc2_1$) which also satisfies the octet rule [12], or the presence of exchange defects II_{IV} and IV_{II} can be tolerated and allows for some disorder tuning of the gap [13–16].

The design flexibility is further enhanced by considering mixed II-IV-N₂ with III-N alloy systems. Recently, the ZnGeN₂-GaN alloy system was investigated both computationally[17] and experimentally in thin film growth[18, 19]. In particular, it was found that at 50% two octet-rule preserving structures can be constructed theoretically with space groups $Pmn2_1$ and $P1n1$, of which the former was found to have the lowest total energy. In the $Pmn2_1$ structure, each N is surrounded by exactly two Ga, one Zn and one Ge and the structure can be viewed as half a layer of ZnGeN₂ and half a layer of GaN in the b direction or a $[010]_{1/2}$ lattice. Experimentally alloys at the 50 % composition were achieved[18] but their detailed structure and degree of ordering is yet to be confirmed. We point out that a line compound at 50 % has been found to exist[20] in the analogous 50 % mixed compound of ZnO and LiGaO₂, which is a mixture of the parent II-VI compound and its ternary I-III-VI₂.

Here we use this flexibility to search for a semiconductor which is closely lattice matched to GaN and has a gap exceeding 4 eV. From, the band gap vs. equivalent wurtzite lattice constant diagram in Ref. 10, one can see that MgSiN₂ is significantly closer lattice matched to GaN than AlN and has a predicted direct gap of ~ 6.3 - 6.5 eV [21, 22]. Unfortunately, its indirect gap is about 0.4 eV lower, so it is actually an indirect gap semiconductor which is undesirable for light emission devices. Upon closer inspection of the lattice match, one should note that the equivalent wurtzite lattice constant in [10] was taken as $a_o/2$. However, inspecting the individual orthorhombic lattice constants, there is only a 1.1% mismatch of MgSiN₂ with respect to $2a_{\text{GaN}}$ in the a -direction, but a -4.7% mismatch in the b direction and a -4% mismatch in the c -direction. Nonetheless, these can be viewed as acceptable lattice mismatch compared with AlN which has a $-2.4, -3.9\%$ mismatch in a and c directions compared to GaN. In particular, a compressive

* ozan.dernek@case.edu

† walter.lambrecht@case.edu

strain in the basal plane would be less disadvantageous than a tensile strain and at least in one basal plane direction, the strain of MgSiN₂ on GaN would be compressive.

The indirect gap in MgSiN₂ results from the valence band maximum (VBM) occurring at $U = (\pi/a, 0, \pi/c)$ in the $Pbn2_1$ setting of the space group, while the conduction band minimum (CBM) occurs at $\Gamma = (0, 0, 0)$. Considering the gap of GaN at U when calculated in an equivalent $Pbn2_1$ supercell, which lies 1.1 eV below the actual VBM at Γ , and interpolating the direct $\Gamma - \Gamma$ and indirect $U - \Gamma$ gaps linearly between MgSiN₂ and GaN, using a direct(indirect) gap of 3.4(4.5) eV in GaN and (6.5,6.1) in MgSiN₂ [21] one might expect a direct gap up to about 75 % and a direct gap of 5.8 eV at that point. Of course, alloy band gaps typically show band gap bowing and the above also ignores strain effects. Nonetheless, this seemed sufficiently promising to investigate the band gap in a quaternary MgSiN₂-GaN system further.

II. COMPUTATIONAL METHOD

The stability of the 50 % alloy is investigated by calculating first the cohesive energy vs. the isolated atoms, second, the enthalpy of formation with respect to the elements in their standard state, and finally, the mixing energy vs. the two end compounds GaN and MgSiN₂. The total energies required for each system are calculated using density functional theory (DFT) within the Generalized Gradient Approximation (GGA) in the Perdew-Burke-Ernzerhof (PBE)[23] parametrization. The structural parameters, internal position and lattice constants were fully relaxed using the QUANTUM ESPRESSO code [24] within the Projector Augmented Wave (PAW) method. Subsequently they were also calculated using the all-electron QUESTAAL code which implements the full-potential linearized muffin-tin orbital (FP-LMTO) method. In evaluating the total energy differences between different systems, we took care of using exactly the same muffin-tin radii for the atoms in different systems and use exactly equivalent \mathbf{k} -point meshes and real space meshes to maximize systematic error cancellation. All, three systems, GaN, MgSiN₂ and MgSiGa₂N₄ were calculated in the same 16 atom cell to achieve equal convergence. The cohesive energy calculations use the single atom energies calculated in large vacuum cells (with spin polarization for Ga, Si and N) and the most stable form of each species. The cohesive energies of the elements were obtained using both code suites and are compared to experimental values in Table I.

The band structures were calculated using the quasi-particle self-consistent (QS) GW approach [25, 26] implemented in the QUESTAAL code[27]. Here GW stands for the one-electron Green's function and W for the screened Coulomb interaction in Hedin's approach [28], which define the self-energy $\Sigma = iGW$. The difference between this non-local and energy dependent self-energy operator

TABLE I: Cohesive energies of each species calculated by QUESTAAL and QE. Species Ga, Mg, and Si are calculated in their bulk phases, and N₂ molecule calculated in a large vacuum cell. Spin-polarization is included for single atom calculations in QE.

Species	Space Group	Coh. En. (eV/atom)		
		QUESTAAL	QE	Expt.
Ga	$Cmce$	-2.69	-2.71	-2.81
Mg	$P6_3/mmc$	-1.50	-1.50	-1.51
Si	$Fd\bar{3}m$	-4.56	-4.62	-4.63
N	N ₂	-5.04	-5.18	-4.92

$\Sigma(\omega)$ and the exchange-correlation potential v_{xc} is, as usual, calculated within first-order perturbation theory starting from the DFT Kohn-Sham (KS) eigenvalues ϵ_i and eigenstates ψ_i . However, in the QS approach, a new energy independent but non-local potential, expressed by its matrix elements in the basis of KS eigenstates, $\tilde{\Sigma}_{ij} = \frac{1}{2}\text{Re}[\Sigma_{ij}(\epsilon_i) + \Sigma_{ij}(\epsilon_j)]$ is evaluated and iterated to convergence. Here $\text{Re}[\dots]$ means taking the hermitian part. The eigenvalues thereby become independent of the DFT starting point exchange-correlation choice. They are found to be typically somewhat overestimating band gaps because within standard GW the screening of the Coulomb potential is calculated in the random phase approximation (RPA) which underestimates screening. This can be overcome by adding ladder diagrams[29-31] but, as a computationally less demanding alternative, it is found that using 80% of the $\tilde{\Sigma}$ and 20% DFT exchange correlation potential usually gives very accurate results for a wide variety of systems[32, 33]. We follow this approach here.

The QUESTAAL implementation of the GW approach uses a mixed interstitial plane wave, product basis set to expand two-point quantities, such as $W = (1 - vP)^{-1}v$, with v the bare Coulomb interaction and $P = -iGG$, the polarization propagator. This is a more efficient basis set than plane waves to represent the screening and, as a result, high-energy states of the KS equation are less crucial to the convergence of the method. The use of an atom-centered basis set allows one to express the self-energy $\tilde{\Sigma}$ in real space and hence to interpolate for \mathbf{k} -point different from the ones for which $\Sigma(\mathbf{k}, \omega)$ is calculated. This way, accurate band dispersions along the symmetry lines and effective masses can be obtained. We tested convergence of the various parameters entering the GW calculations, finding a $3 \times 3 \times 3$ \mathbf{k} -mesh, $spdf - spd$ basis set including Ga-3d local orbitals, and E_{max} above which the self-energy is approximated by an average value to be well converged. Details of the QSGW implementation can be found in Ref.[26].

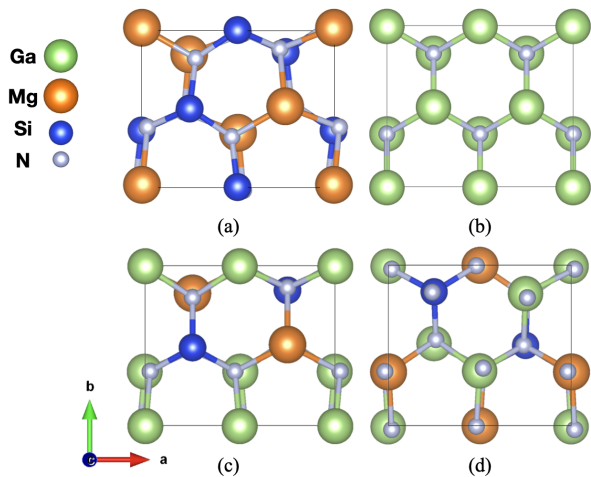


Fig. 1: Octet-rule-preserving $\text{MgSiGa}_2\text{N}_4$ structures in (c) $Pmn2_1$ and (d) $P1n1$ space groups and their relation to the compounds (a) MgSiN_2 and (b) GaN both in the $Pbn2_1$ structure.

III. RESULTS

We here present results for both the $Pmn2_1$ and $P1n1$ structures, shown in Fig. 1, which were both found to have low energy in the $\text{ZnGeGa}_2\text{N}_4$ compound at 50% mixing. We start with the structural parameters, given in Table II. We compare the lattice constants with the Vegard's average. $Pmn2_1$ perfectly matches these values. When all the lattice constants and angles between them are relaxed, the $P1n1$ structure slightly shifts into a monoclinic phase, with the angles between the lattice vectors $\alpha = \gamma = 90^\circ$ and $\beta = 90.16^\circ$. This is consistent with the space group which belongs in the monoclinic crystal system. However, the change in the volume and total energy and the total energy is negligible. Therefore we continue to investigate the material in its orthorhombic phase. The $P1n1$ lattice constant a falls out of the range set by GaN and MgSiN_2 , while b and c are very close to the GaN lattice constants. Yet the volume of the two structures are identical. The reduced coordinates for the atoms in the $Pmn2_1$ and for the $P1n1$ are provided in Appendix A. Compared to experimental values, we may notice that the volume is overestimated by 2.1 % for MgSiN_2 and by 2.8 % for GaN . We thus also expect an overestimate by a similar amount for the 50 % compound.

Next, we discuss the total energy results which allow us to ascertain the stability of the proposed alloy. Table IV lists the cohesive energies, enthalpies of formation and mixing energy all evaluated using both methods. Values obtained by the QE method are given in parentheses. The enthalpies of formation give the energy difference with respect to the elements in their standard state at room temperature and atmospheric pressure. Their negative value indicate stability. A more strict criterion is

to evaluate the mixing energy of the alloy with respect to the two separate compounds. These values are positive but quite small. The positive value indicates, as usual for semiconductor alloys, that there exists a miscibility gap and mixing can only occur above a certain temperature where entropy of mixing makes the Gibbs free energy negative. But once the alloys are formed at the growth temperature, the atomically mixed frozen-in structure is expected to be kinetically stable at lower temperatures. The miscibility gap temperature is directly related to the mixing energy at 50 % composition and this being low indicates a relatively small driving force toward phase segregation and a low mixing temperature. The energy of mixing reported here assumes perfect satisfaction of the octet rule and is thus a lower limit of the mixing enthalpy in a more realistic alloy structure, which may be expected to have a certain degree of disorder, in particular short-range disorder involving local motifs around the N anion deviating from the perfect Ga_2MgSi by either excess Ga, excess Mg or excess Si. The study of these defects and their energy cost is a topic that needs to be addressed in future research.

Subsequently, we calculated their electronic band structures both in GGA and in the quasiparticle self-consistent GW approximations. The results of the band gaps are included in Table V. The band gaps here do not include zero-point motion electron-phonon coupling corrections. In Ref. 21 these were estimated to be of order -0.2 eV. On the other hand, the overestimate of the volume by about 2 % leads to an underestimate of the band gap. Using the band gap deformation potential $dE_g/d\ln V$ of -8.7 eV [21], the volume correction would increase the gap by about 0.2 eV. Thus these two corrections nearly cancel each other. For GaN , likewise, our gap here is underestimated by about 0.2-0.3 eV because of our use here of the GGA volume. The band structures are shown in Fig 2. The overview band structure shows that the top set of valence bands between -8 and 0 eV are predominantly N-2p like as expected for a nitride. These show projections on the local partial waves. Near the bottom of the valence band we can see that the states are bonding between N-2p and Si-s and Ga-s. The Mg-s contribution is less strongly present. The conduction band minimum atomic orbital character is more readily seen in the colored bands which indicate the contribution of the Ga-s muffin-tin-orbital basis functions. The corresponding Si-s and Mg-s are not shown but are significantly smaller. The predominant Ga-s rather than Mg or Si-s character of the CBM is consistent with a quantum well model. The $Pmn2_1$ is essentially an ultra-thin superlattice of half unit cell GaN quantum wells and half unit cell MgSiN_2 units stacked along the \mathbf{b} -direction. The band offset is type I with a conduction band off set of about 1.4 eV according to Ref. [34] and hence if the quantum well just captures a single bound state, it could be at about 1.4 eV above the GaN CBM. The quantum confined effects for the holes are expected to be smaller since the effective masses are much larger. The wider the

TABLE II: Average bond lengths and relaxed lattice constants in Å for compounds and $\text{MgSiGa}_2\text{N}_4$ structures. Unit cell volumes are compared with the Vegard's average of MgSiN_2 and GaN.

	Mg-N (Å)	Ga-N (Å)	Si-N (Å)	a (Å)	b (Å)	c (Å)	Volume (Å ³)
MgSiN_2	2.11		1.76	6.504	5.310	5.031	173.75
Expt. ^a	2.09		1.75	6.473	5.272	4.986	170.15
GaN		1.96		6.433	5.571	5.240	187.79
Expt. ^b		1.95		6.378	5.523	5.185	182.65
$Pmn2_1$	2.06	1.95	1.75	6.467	5.440	5.147	181.07
$P1n1$	2.04	1.95	1.75	6.324	5.550	5.159	181.07
Vegard's				6.469	5.441	5.136	180.75

^a R.J. Bruls, H. T. Hintzen, R. Metselaar, and C. Loong J. Phys. Chem. Solids 61 1285.

^b T. Detchprohm, K.Hiramatsu, K. Itoh, I. Akasaki Jpn. J. Appl. Phys. (Japan), vol. 25 (1986), p. L1454-6

TABLE III: Band gaps of compounds and alloys in various approximations.

Compound		GGA	0.8Σ	$0.8\Sigma + \Delta(0)^a$
MgSiN_2	Indirect	4.03	6.15	5.84
MgSiN_2	Direct	4.36	6.52	6.28
GaN	Direct	1.72	3.08	
$\text{MgSiGa}_2\text{N}_4$ ($Pmn2_1$)	Direct	2.98	4.83	
$\text{MgSiGa}_2\text{N}_4$ ($Pmn2_1$)	Indirect	2.92	4.76	
$\text{MgSiGa}_2\text{N}_4$ ($P1n1$)	Direct	2.73	4.60	
$\text{MgSiGa}_2\text{N}_4$ ($P1n1$)	Indirect	2.70	4.57	

^a $\Delta(0)$ is an estimated zero-point motion correction from Ref. [21]

TABLE IV: Cohesive energies, energy of formation, and mixing energies in GGA with units eV/atom. The values given in parenthesis are obtained by the QE method, the other ones by QUESTAAL.

	MgSiN_2	GaN	$Pmn2_1$	$P1n1$
E_{coh}	5.25 (5.31)	4.39 (4.42)	4.82 (4.86)	4.80 (4.84)
E_{for}	-1.19 (-1.19)	-0.52 (-0.47)	-0.90 (-0.83)	-0.88 (-0.81)
E_{mix}			0.008 (0.007)	0.029 (0.031)

barrier of MgSiN_2 in this case, the stronger the quantum confinement effects would be and hence the larger the gap of the $(\text{MgSiN}_2)_x(\text{GaN})_{1-x}$ alloys.

A zoom in near the VBM and CBM for both structures shows that the VBM does not occur at Γ but rather at Y , $(0, \pi/2b, 0)$, and thus, strictly speaking, we still have an indirect gap system. However, this location of the VBM is different from that of MgSiN_2 , where it occurs at U , $(\pi/2a, 0, \pi/2c)$, and the energy difference between the VBM at Γ and Y here is very small. Furthermore, this is expected to be rather sensitive to strain. It also shows details of the crystal field splitting at Γ in $Pmn2_1$ structure. The PDOS in the CBM shows that near the CBM the N- s partial waves dominate over the cation- s states but we should recall that these are anti-bonding s states and that the dominant Ga- s muffin-tin-orbital (as shown from the band color) extends into the N spheres

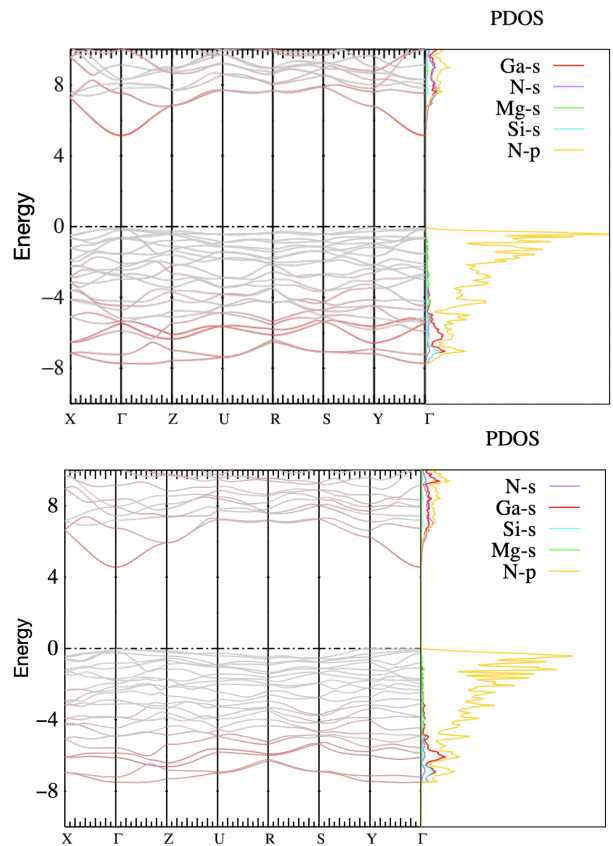


Fig. 2: Band structures and corresponding partial density of states are shown for both $Pmn2_1$ (top) and $P1n1$ (bottom) space group of $\text{MgSiGa}_2\text{N}_4$ alloy. The band structures are calculated in the 0.8Σ approximation, and Ga- s orbitals are color coded with red-scale while the rest of the orbitals are in gray-scale. In both structures, the VBM is found to be on the k-point Y , but the difference between the VBM and highest valence band energy at Γ is less than 0.1 eV (Table V). Partial density of states (in arbitrary but consistent units of states/cell per eV) are given for the orbitals of interest. The valence bands are dominated by the N- p orbitals (color gold), while the CBM consists of mostly Ga- s orbitals (color red).

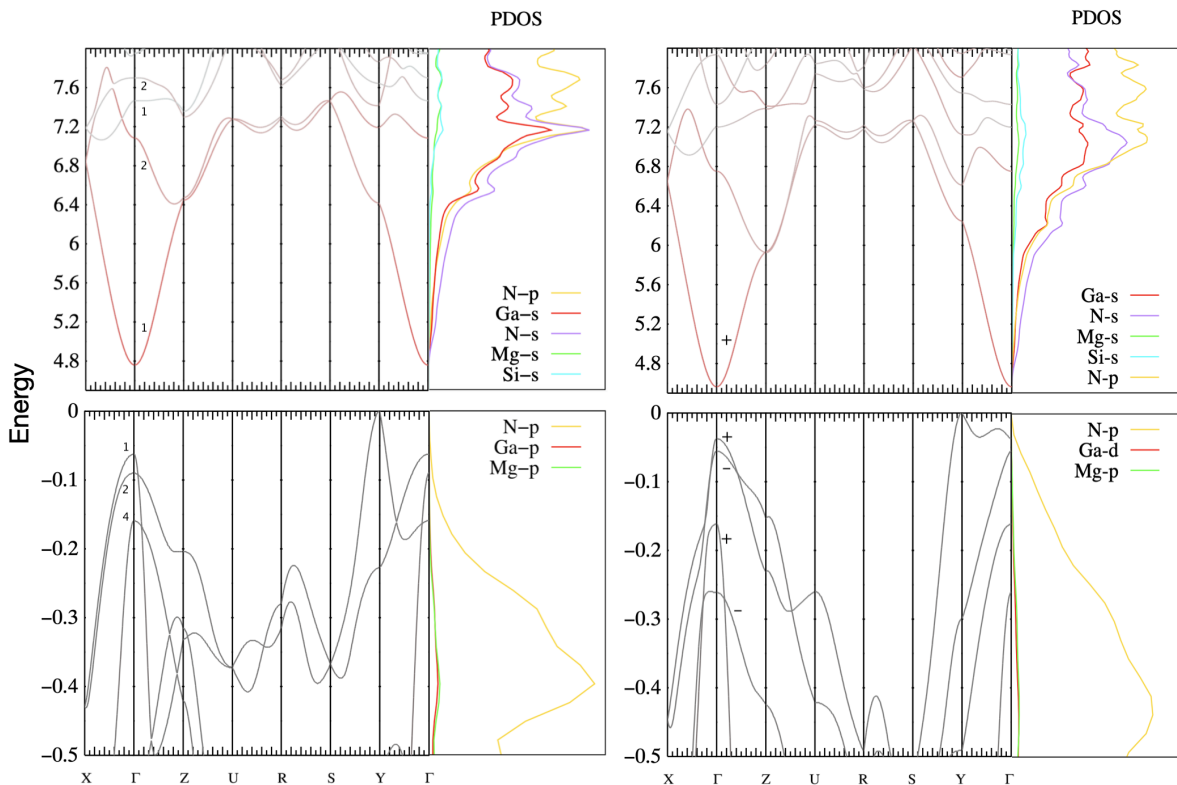


Fig. 3: Band splitting and their symmetries are shown for $Pmn2_1$ (left) and $P1n1$ (right) structures, along with the partial density of states of dominant orbitals. Same color coding as in Fig. 2 is used.

TABLE V: Band gaps of compounds and alloys in various approximations.

Compound		GGA	0.8Σ	$0.8\Sigma + \Delta(0)^a$
MgSiN ₂	Indirect	4.03	6.15	5.84
MgSiN ₂	Direct	4.36	6.52	6.28
GaN	Direct	1.72	3.08	
MgSiGa ₂ N ₄ ($Pmn2_1$)	Direct	2.98	4.83	
MgSiGa ₂ N ₄ ($Pmn2_1$)	Indirect	2.92	4.76	
MgSiGa ₂ N ₄ ($P1n1$)	Direct	2.73	4.60	
MgSiGa ₂ N ₄ ($P1n1$)	Indirect	2.70	4.57	

^a $\Delta(0)$ is an estimated zero-point motion correction from Ref. [21]

and these thus also contribute to the N-s PDOS.

The bands at Γ were symmetry labeled for $Pmn2_1$. The point group is C_{2v} . In this point group, Γ_1 (or a_1) correspond to the z basis function with x, y, z along (a, b, c) respectively, Γ_2 corresponds to b_2 or y and Γ_4 to b_1 or x . The a_2 or Γ_3 corresponds to xy basis function. The CBM has Γ_1 symmetry and is s -like. Thus allowed dipole transitions occur between the VBM at Γ and the CBM for $\mathbf{E} \parallel \mathbf{c}$. For $\mathbf{E} \parallel \mathbf{b}$ the transitions occur from the second VBM, and for $\mathbf{E} \parallel \mathbf{a}$ they occur for the third VBM. The valence band splittings are given in Table VI. We may also note that the z -like Γ_1 state has the smallest mass along the $\Gamma - Z$ direction, while the next Γ_2

or y -like state has the smallest mass in the $\Gamma - Y$ direction and the Γ_4 or x -like state has its lowest mass in the $\Gamma - X$ direction. Unfortunately, the top of the VBM is thus z -like which implies that the same problem occurs as for $\text{Al}_x\text{Ga}_{1-x}\text{N}$ at high Al-concentration x . Namely, the lowest energy transition is predominantly transverse magnetic (TM) which hinders light extraction for normal exit angle from the basal plane. However, this is sensitive to strain and the splitting between the Γ_2 and Γ_1 state is quite small and could perhaps more easily be reversed by some strain engineering. Also, it might be possible to grown these materials as films with other surfaces than the basal plane, in which case the \mathbf{c} -axis would be in the plane.

For the $P1n1$ -structure, we have only a double-glide mirror plane n perpendicular to the b -axis, so the point group is C_s and states can only be labeled even or odd with respect to the mirror n_y mirror-plane. Obviously, y orbitals are odd with respect to this mirror-plane while x and z are even. We can see some interesting changes in the band structure reflecting the lower symmetry. First, at Γ , there are now four states instead of three within the first 0.3 eV below the VBM. Along the $\Gamma - X$ line we can see that the top two bands cross, indicating that they have different irreducible representations, respectively $+$ and $-$. The next band down has $+$ symmetry and therefore an avoided crossing with the $+$ band emanating from the VBM at Γ . Along $\Gamma - Y$ however, there is no sym-

metry left at all and hence the top bands can repel each other while in the $Pmn2_1$ these bands were allowed to cross because of their different even or odd character with respect to the m_x mirror plane.

We have also determined the effective mass tensors at the band edges, as given in Table VII. The curvatures are determined by fitting the bands to a parabolic dispersion very close to the band edge in question in several directions and subsequently determining the principal values and direction of the constant energy surfaces. The conduction band mass tensor shows only slight anisotropy consistent with the point group symmetry. In the $P1n1$ case, one principal axis is along y , the other two can be at some angle from x in the xz plane because the point group is only C_s . For the CBM, we find these angles to be near 45° . The three highest valence bands at Γ show a larger anisotropy with the smallest negative mass occurring in the direction that corresponds to the irreducible representation of the band in question. In terms of the well known $\mathbf{k} \cdot \mathbf{p}$ expression for the inverse effective mass tensor,

$$M_{\alpha\beta}^{-1} = \delta_{\alpha\beta} \frac{1}{m_e} + \frac{1}{m_e^2} \sum_{n' \neq n} \frac{\langle n\mathbf{k}|p_\alpha|n'\mathbf{k}\rangle \langle n'\mathbf{k}|p_\beta|n\mathbf{k}\rangle + c.c.}{E_{n\mathbf{k}} - E_{n'\mathbf{k}}} \quad (1)$$

we can see that the interaction of the top valence band with the conduction band would give a small negative contribution to the M_{zz}^{-1} and none at all for M_{xx}^{-1} or M_{yy}^{-1} because only p_z matrix elements can couple the VBM of Γ_1 symmetry to the Γ_1 CBM. On the other hand in the x (y) directions, there are valence band states just below it of symmetry Γ_4 (Γ_2) which will couple to the VBM of Γ_1 symmetry and hence give a large positive change in M_{xx}^{-1} or M_{yy}^{-1} . This means a large negative change in the mass itself because $\Delta(1/m) = -\Delta m/m^2$. Thus we find strongly negative masses for the x and y directions for the Γ_1 VBM. This implies a high positive hole mass in these directions. Other lower lying Γ_1 states will also give a negative contribution to the effective mass in the z direction but, because these states are farther away, they will result in a smaller negative mass in the z direction. Similar reasoning explains the other cases. For the Γ_2 second valence band, the Γ_1 state above it which is the smallest energy difference, will give a strong negative contribution to M_{yy}^{-1} in the $\Gamma - Y$ direction so a positive change to the mass itself which must compensate the effect from bands of Γ_1 symmetry lying deeper in the valence band. Hence the smallest mass along the y direction for the state of Γ_2 or y symmetry. For the $P1n1$ case, the top valence band along y is seen to have a positive curvature because of the strong repulsion of the two two valence bands along this symmetry line. For the mass tensor at Y we can see for $Pmn2_1$ that $(m_x m_y m_z)^{1/3} = 1.09$, so the effectively average density of states mass is close the free electron mass. For the $P1n1$ structure the effective density of states mass is 1.48, thus somewhat higher. While the conduction band masses are similar and again nearly isotropic.

TABLE VI: Valence-band splittings (in meV) at the Γ point relative to actual VBM at Y .

Symmetry	$Pmn2_1$	Symmetry	$P1n1$
Γ_1	-63	+	-37
Γ_2	-90	-	-56
Γ_4	-159	+	-162
		-	-261

TABLE VII: Electron effective masses (in units of free electron mass m_e) at Γ for CBM and top valence bands in close vicinity to VBM are given for $Pmn2_1$ and $P1n1$ structures. The mass tensor components at the true VBM at Y are also given. The negative values for valence bands indicate positive hole masses. For the orthorhombic case ($Pmn2_1$), the principal axes are along the crystal axes x, y, z corresponding to a, b, c ; for the $P1n1$ monoclinic space group, one principal axis is along y , the others in the xz plane make an angle α_x from the x axis as indicated.

	CBM	Γ_1	Γ_4	Γ_2	Y	
m_x	0.244	-3.059	-0.224	-4.321	-0.714	
m_y	0.257	-11.302	-3.887	-0.272	-1.105	
m_z	0.226	-0.196	-2.567	-2.494	-1.666	
	CBM	$+_1$	$-_1$	$+_2$	$-_2$	Y
m_1	0.243	-0.286	-0.459	-0.196	-2.372	-0.664
α_x	-43.6	2.5	-3.7	91.2	-87.8	0.5
m_2	0.240	-2.988	-3.936	-2.652	-2.652	-1.627
α_x	46.4	92.5	86.3	1.2	2.2	89.5
m_y	0.264	2.167	-0.948	-2.348	-0.251	-3.025

Finally, we make an estimate of the band gap bowing in the alloy system. The band gap is estimated as $E_g(x) = E_g(0) + xE_g(1) - bx(1-x)$. For the direct $\Gamma - \Gamma$ gap we find $b \approx 0.6$ eV, while for the $U - \Gamma$ gap is it about 0.7 eV. The results are shown in Fig. 4. They show that a band crossing between direct and indirect gap still occurs at about $x = 0.75$ with a gap as high as 5.6 eV at this point. We note that in principle, octet-rule conserving superlattice type structures with half unit cells of $MgSiN_2$ and GaN stacked along the b direction as building blocks can be designed.[17] However, in a more disordered alloy system, one may expect some octet-rule violating motifs to exist, in particular those that involve a change in local valence by only ± 1 . Their presence would likely decrease the gap by creating a tail of defect related states in the gap near the band edges. From related ternary compounds such as $ZnGeN_2$ we expect these to reduce the gap by about 0.5 ± 0.2 eV. This would still leave a nearly direct gap larger than 4 eV but with a larger band gap bowing of $b \approx 2.6$. In such a more disordered system, the distinction between the slightly lower indirect gap $Y - \Gamma$ and the direct gap would become essentially wiped out by the disorder induced band broadening.

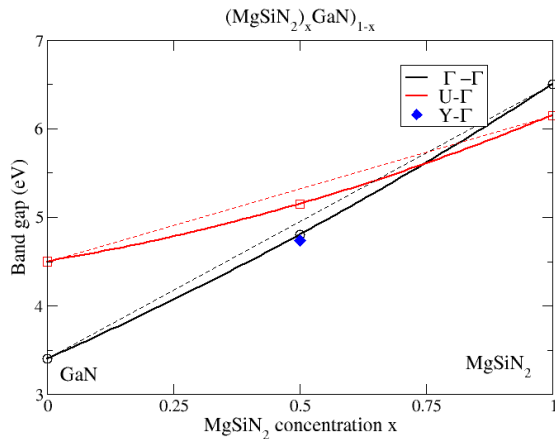


Fig. 4: Band gaps in the $(\text{MgSiN}_2)_x(\text{GaN})_{1-x}$ alloy system.

IV. CONCLUSIONS

We have shown that a 50 % alloy of MgSiN_2 and GaN is promising as an alternative to $\text{Al}_x\text{Ga}_{1-x}\text{N}$ alloy for increasing the gap beyond that of GaN to allow for optoelectronic applications into the deep UV region. First, we find that two octet-ruling compounds exist with the composition $\text{MgSiGa}_2\text{N}_4$ which have negative energies of formation and only a small positive mixing energy with respect to GaN and MgSiN_2 . While we expect octet-rule violating motifs to increase the mixing energy we still expect such alloys to be feasible. In its lowest energy structure with space group $Pmn2_1$, the lattice constant in the a direction has only a +0.5 % mismatch with the corresponding lattice constant in GaN and the positive sign indicates that on a GaN substrate this compound would be under compression in this direction. In the other direction in the basal plane, its mismatch is -2.3%. The band gap of this structure is nearly direct, by which we mean that the direct gap is less than 0.1 eV below the direct gap at Γ , and the direct gap is calculated to be 4.83 eV. Another structure with space group $P1n1$ also has fairly good lattice mismatch from GaN and a nearly direct gap of 4.76 eV. These small deviations from direct gap character could possibly be overcome by strain tuning.

We should point out some caveats here. For a quaternary system, achieving the precise $Pmn2_1$ ordering is even more challenging than for a ternary and going away from the perfect 50% stoichiometry of MgSiN_2 - $(\text{GaN})_2$ would likely introduce even more cation disorder in the form of locally octet-rule violating motifs. This is expected to decrease the band gap somewhat but a direct gap larger than 4 eV is still expected. On the other hand, octet-rule satisfying superlattices at different concentra-

tions are in principle possible and may provide higher gaps but are even more challenging to achieve. To facilitate comparison with future experimental realization of these materials we have provided ample detail on their predicted crystal structure and band structure, including the effective mass tensors at the band edges.

ACKNOWLEDGMENTS

The calculations were performed on the High Performance Computing Resource in the Core Facility of Advanced Research Computing at Case Western Reserve University. This work was supported by the US Department of Energy Basic Energy Sciences (DOE-BES) under grant number DE-SC0008933.

Appendix A: Structural detail

The reduced coordinates of the atoms and their Wyckoff designation are given in Tables VIII, IX for $Pmn2_1$ and $P1n1$ respectively.

TABLE VIII: Reduced coordinates of atoms for the $Pmn2_1$ structure.

Atom	Wyckoff ^a	x	y	z
Ga	4b	0.25162	-0.32950	0.49925
Mg	2a	0.00000	0.16007	0.49196
Si	2a	0.00000	-0.17887	0.00043
N_{Ga}	4b	0.22286	-0.32754	0.88188
N_{Mg}	2a	0.00000	0.13495	0.90272
N_{Si}	2a	0.00000	-0.19564	0.34264

^a $2a$ positions are (x,y,z) and $(1/2,-y,z+1/2)$, $4b$ positions are (x,y,z) , $(-x+1/2,-y,z+1/2)$, $(x+1/2,-y,z+1/2)$, and $(-x,y,z)$.

TABLE IX: Reduced coordinates of atoms for the $P1n1$ structure.

Atom	Wyckoff ^a	x	y	z
Ga_1	2a	0.49984	-0.15530	-0.00064
Ga_2	2a	0.74905	-0.32606	0.49904
Mg	2a	0.25124	-0.33223	0.49367
Si	2a	0.00024	-0.16716	0.00067
$\text{N}_{\text{Ga}1}$	2a	0.50965	-0.13049	0.38153
$\text{N}_{\text{Ga}2}$	2a	0.26846	0.30852	0.38142
N_{Mg}	2a	0.73140	0.32936	0.40271
N_{Si}	2a	-0.00986	-0.16526	0.34159

^a All atoms in $2a$ positions: (x,y,z) , $(-x+1/2,-y,z+1/2)$

- [1] M. Kneissl, T.-Y. Seong, J. Han, and H. Amano, The emergence and prospects of deep-ultraviolet light-emitting diode technologies, *Nature Photonics* **13**, 233 (2019).
- [2] M. Crawford, Chapter One - Materials Challenges of AlGa_N-Based UV Optoelectronic Devices, in *III-Nitride Semiconductor Optoelectronics*, Semiconductors and Semimetals, Vol. 96, edited by Z. Mi and C. Jagadish (Elsevier, 2017) pp. 3–44.
- [3] T. Detchprohm, X. Li, S.-C. Shen, P. Yoder, and R. Dupuis, Chapter Four - III-N Wide Bandgap Deep-Ultraviolet Lasers and Photodetectors, in *III-Nitride Semiconductor Optoelectronics*, Semiconductors and Semimetals, Vol. 96, edited by Z. Mi and C. Jagadish (Elsevier, 2017) pp. 121–166.
- [4] M. Shatalov, R. Jain, T. Saxena, A. Dobrinsky, and M. Shur, Chapter Two - Development of Deep UV LEDs and Current Problems in Material and Device Technology, in *III-Nitride Semiconductor Optoelectronics*, Semiconductors and Semimetals, Vol. 96, edited by Z. Mi and C. Jagadish (Elsevier, 2017) pp. 45–83.
- [5] H. Hirayama, Chapter Three - Growth of High-Quality AlN on Sapphire and Development of AlGa_N-Based Deep-Ultraviolet Light-Emitting Diodes, in *III-Nitride Semiconductor Optoelectronics*, Semiconductors and Semimetals, Vol. 96, edited by Z. Mi and C. Jagadish (Elsevier, 2017) pp. 85–120.
- [6] S. Zhao and Z. Mi, Chapter Five - Al(Ga)_N Nanowire Deep Ultraviolet Optoelectronics, in *III-Nitride Semiconductor Optoelectronics*, Semiconductors and Semimetals, Vol. 96, edited by Z. Mi and C. Jagadish (Elsevier, 2017) pp. 167–199.
- [7] J. Zhang, H. Zhao, and N. Tansu, Effect of crystal-field split-off hole and heavy-hole bands crossover on gain characteristics of high Al-content AlGa_N quantum well lasers, *Applied Physics Letters* **97**, 111105 (2010).
- [8] C. Reich, M. Guttman, M. Feneberg, T. Wernicke, F. Mehnke, C. Kuhn, J. Rass, M. Lapeyrade, S. Einfeldt, A. Knauer, V. Kueller, M. Weyers, R. Goldhahn, and M. Kneissl, Strongly transverse-electric-polarized emission from deep ultraviolet AlGa_N quantum well light emitting diodes, *Applied Physics Letters* **107**, 142101 (2015).
- [9] W. R. L. Lambrecht and A. Punya, Heterovalent ternary II-IV-N₂ compounds: perspectives for a new class of wide-band-gap nitrides, in *III-Nitride Semiconductors and their Modern Devices*, edited by B. Gill (Oxford University Press, 2013) Chap. 15, pp. 519–585.
- [10] S. Lyu, D. Skachkov, K. Kash, E. W. Blanton, and W. R. L. Lambrecht, Band gaps, band-offsets, disorder, stability region, and point defects in II-IV-n₂ semiconductors, *Physica Status Solidi (a)* **216**, 1800875 (2019).
- [11] A. D. Martinez, A. N. Fioretti, E. S. Toberer, and A. C. Tamboli, Synthesis, structure, and optoelectronic properties of II-IV-V₂ materials, *J. Mater. Chem. A* **5**, 11418 (2017).
- [12] P. C. Quayle, E. W. Blanton, A. Punya, G. T. Junno, K. He, L. Han, H. Zhao, J. Shan, W. R. L. Lambrecht, and K. Kash, Charge-neutral disorder and polytypes in heterovalent wurtzite-based ternary semiconductors: The importance of the octet rule, *Phys. Rev. B* **91**, 205207 (2015).
- [13] D. Skachkov, P. C. Quayle, K. Kash, and W. R. L. Lambrecht, Disorder effects on the band structure of ZnGeN₂: Role of exchange defects, *Phys. Rev. B* **94**, 205201 (2016).
- [14] S. Lany, A. N. Fioretti, P. P. Zawadzki, L. T. Schelhas, E. S. Toberer, A. Zakutayev, and A. C. Tamboli, Monte Carlo simulations of disorder in ZnSnN₂ and the effects on the electronic structure, *Phys. Rev. Materials* **1**, 035401 (2017).
- [15] J. J. Cordell, G. J. Tucker, A. Tamboli, and S. Lany, Bandgap analysis and carrier localization in cation-disordered ZnGeN₂, *APL Materials* **10**, 011112 (2022).
- [16] T. D. Veal, N. Feldberg, N. F. Quackenbush, W. M. Linhart, D. O. Scanlon, L. F. J. Piper, and S. M. Durbin, Band Gap Dependence on Cation Disorder in ZnSnN₂ Solar Absorber, *Advanced Energy Materials* **5**, 1501462 (2015).
- [17] B. H. D. Jayatunga, S. Lyu, S. K. Radha, K. Kash, and W. R. L. Lambrecht, Ordering in the mixed ZnGeN₂-Ga_N alloy system: Crystal structures and band structures of ZnGeGa₂N₄ from first principles, *Phys. Rev. Materials* **2**, 114602 (2018).
- [18] B. H. D. Jayatunga, M. R. Karim, R. A. Lalk, O. Ohanaka, W. R. L. Lambrecht, H. Zhao, and K. Kash, Metal-Organic Chemical Vapor Deposition of ZnGeGa₂N₄, *Crystal Growth & Design* **20**, 189 (2020).
- [19] T. Suehiro, M. Tansho, and T. Shimizu, Quaternary Wurtzitic Nitrides in the System ZnGeN₂-Ga_N: Powder Synthesis, Characterization, and Potentiality as a Photocatalyst, *The Journal of Physical Chemistry C* **121**, 27590 (2017).
- [20] T. Omata, M. Kita, K. Nose, K. Tachibana, and S. Otsuka-Yao-Matsuo, Zn₂LiGaO₄, Wurtzite-Derived Wide Band Gap Oxide, *Japanese Journal of Applied Physics* **50**, 031102 (2011).
- [21] A. P. Jaroenjittichai and W. R. L. Lambrecht, Electronic band structure of Mg-IV-n₂ compounds in the quasiparticle-self-consistent *gw* approximation, *Phys. Rev. B* **94**, 125201 (2016).
- [22] J. B. Quirk, M. Räsander, C. M. McGilvery, R. Palgrave, and M. A. Moram, Band gap and electronic structure of MgSiN₂, *Applied Physics Letters* **105**, 112108 (2014).
- [23] J. P. Perdew, K. Burke, and M. Ernzerhof, Generalized gradient approximation made simple, *Phys. Rev. Lett.* **77**, 3865 (1996).
- [24] P. Giannozzi, S. Baroni, N. Bonini, M. Calandra, R. Car, C. Cavazzoni, D. Ceresoli, G. L. Chiarotti, M. Cococcioni, I. Dabo, A. Dal Corso, S. de Gironcoli, S. Fabris, G. Fratesi, R. Gebauer, U. Gerstmann, C. Gougoussis, A. Kokalj, M. Lazzeri, L. Martin-Samos, N. Marzari, F. Mauri, R. Mazzarello, S. Paolini, A. Pasquarello, L. Paulatto, C. Sbraccia, S. Scandolo, G. Sclauzero, A. P. Seitsonen, A. Smogunov, P. Umari, and R. M. Wentzcovitch, Quantum espresso: a modular and open-source software project for quantum simulations of materials, *Journal of Physics: Condensed Matter* **21**, 395502 (19pp) (2009).
- [25] M. van Schilfgaarde, T. Kotani, and S. Faleev, Quasiparticle Self-Consistent *GW* Theory, *Phys. Rev. Lett.* **96**, 226402 (2006).
- [26] T. Kotani, M. van Schilfgaarde, and S. V. Faleev, Quasiparticle self-consistent *GW* method: A basis for the

- independent-particle approximation, Phys.Rev. B **76**, 165106 (2007).
- [27] D. Pashov, S. Acharya, W. R. Lambrecht, J. Jackson, K. D. Belashchenko, A. Chantis, F. Jamet, and M. van Schilfgaarde, Questaal: A package of electronic structure methods based on the linear muffin-tin orbital technique, Computer Physics Communications, 107065 (2019).
- [28] L. Hedin, New method for calculating the one-particle green's function with application to the electron-gas problem, Phys. Rev. **139**, A796 (1965).
- [29] B. Cunningham, M. Grüning, P. Azarhoosh, D. Pashov, and M. van Schilfgaarde, Effect of ladder diagrams on optical absorption spectra in a quasiparticle self-consistent GW framework, Phys. Rev. Materials **2**, 034603 (2018).
- [30] B. Cunningham, M. Grüning, D. Pashov, and M. van Schilfgaarde, QSGW: Quasiparticle Self consistent GW with ladder diagrams in W (2021), preprint arXiv 2106.05759.
- [31] S. K. Radha, W. R. L. Lambrecht, B. Cunningham, M. Grüning, D. Pashov, and M. van Schilfgaarde, Optical response and band structure of LiCoO_2 including electron-hole interaction effects, Phys. Rev. B **104**, 115120 (2021).
- [32] C. Bhandari, M. van Schilfgaarde, T. Kotani, and W. R. L. Lambrecht, All-electron quasiparticle self-consistent GW band structures for SrTiO_3 including lattice polarization corrections in different phases, Phys. Rev. Materials **2**, 013807 (2018).
- [33] D. Deguchi, K. Sato, H. Kino, and T. K. Ni, Accurate energy bands calculated by the hybrid quasiparticle self-consistent GW method implemented in the ecalj package, Japanese Journal of Applied Physics **55**, 051201 (2016).
- [34] S. Lyu and W. R. L. Lambrecht, Band alignment of III-N, ZnO and II-IV-N₂ semiconductors from the electron affinity rule, Journal of Physics D: Applied Physics **53**, 015111 (2019).